JBC RESEARCH ARTICLE

Single-domain antibodies neutralize ricin toxin intracellularly by blocking access to ribosomal P-stalk proteins

Received for publication, January 22, 2022, and in revised form, February 10, 2022 Published, Papers in Press, February 17, 2022,
https://doi.org/10.1016/j.jbc.2022.101742

Timothy F. Czajka[1], David J. Vance[1,2], Simon Davis[3], Michael J. Rudolph[3,*], and Nicholas J. Mantis[1,2,*]

From the [1]Department of Biomedical Sciences, University at Albany, Albany, New York, USA; [2]Division of Infectious Diseases, Wadsworth Center, New York State Department of Health, Albany, New York, USA; [3]New York Structural Biology Center, New York, New York, USA

Edited by Peter Cresswell

During ricin intoxication in mammalian cells, ricin's enzymatic (RTA) and binding (RTB) subunits disassociate in the endoplasmic reticulum. RTA is then translocated into the cytoplasm where, by virtue of its ability to depurinate a conserved residue within the sarcin–ricin loop (SRL) of 28S rRNA, it functions as a ribosome-inactivating protein. It has been proposed that recruitment of RTA to the SRL is facilitated by ribosomal P-stalk proteins, whose C-terminal domains interact with a cavity on RTA normally masked by RTB; however, evidence that this interaction is critical for RTA activity within cells is lacking. Here, we characterized a collection of single-domain antibodies (V_HHs) whose epitopes overlap with the P-stalk binding pocket on RTA. The crystal structures of three such V_HHs (V9E1, V9F9, and V9B2) in complex with RTA revealed not only occlusion of the ribosomal P-stalk binding pocket but also structural mimicry of C-terminal domain peptides by complementarity-determining region 3. *In vitro* assays confirmed that these V_HHs block RTA–P-stalk peptide interactions and protect ribosomes from depurination. Moreover, when expressed as "intrabodies," these V_HHs rendered cells resistant to ricin intoxication. One V_HH (V9F6), whose epitope was structurally determined to be immediately adjacent to the P-stalk binding pocket, was unable to neutralize ricin within cells or protect ribosomes from RTA *in vitro*. These findings are consistent with the recruitment of RTA to the SRL by ribosomal P-stalk proteins as a requisite event in ricin-induced ribosome inactivation.

Ricin toxin is the archetype of the large and diverse family of medically important plant and bacterial ribosome-inactivating proteins (RIPs). A byproduct of castor beans (*Ricinus communis*), ricin toxin consists of two equal sized subunits, ricin toxin A subunit (RTA) and ricin toxin B subunit (RTB), that associate through electrostatic and covalent interactions (1, 2). RTB is a bivalent Gal/GalNAc-specific lectin that traffics RTA from the plasma membrane to the endoplasmic reticulum (ER) (3). Within the ER, the interchain disulfide bond linking RTA and RTB is reduced by protein disulfide isomerase, and RTA is then retrotranslocated in an unfolded state across the ER membrane and into the cytoplasm (4–7). From that point forward, RTA functions as a RIP, triggering the ribotoxic stress response and programmed cell death pathways (8–11).

The mode of action of RTA in inactivating mammalian ribosomes is well established. RTA catalyzes the hydrolysis of the *N*-glycosidic bond of a single adenine base within the sarcin–ricin loop (SRL) of the 28S rRNA, a conserved hairpin-like structure that interacts with eukaryotic elongation factors (EFs) 1 and 2, during ribosome translocation (1, 2, 9, 12–16). The active site of RTA consists of a large solvent-exposed cleft on one face of the molecule that accommodates adenine through a π-stacking network and hydrogen bonding (16, 17). Site-directed mutagenesis has identified the key residues within the active site that are associated with RNA *N*-glycosidase activity (18). Namely, Tyr-80 and Tyr-123 stabilize the incoming adenine base *via* a π-stacking network, whereas Arg-180 is involved in protonation of the adenine-leaving group. Glu-177 participates in the ultimate hydrolysis of the *N*-glycosidic bond. There is neither evidence that residues outside the active site properly contribute to SRL depurination nor are there any reports that RTA enzyme kinetics are subject to allostery.

That said, there is a growing body of evidence that SRL depurination is the second event in a two-step interaction between RTA and the ribosome (19, 20). According to the two-step model, RTA first associates with the C terminus of the acidic P-stalk proteins (RPLP1 and RPLP2; "P1" and "P2") of the 60S ribosome before being guided to the SRL (20–22). Targeted mutagenesis identified residues along the face of RTA normally occluded by RTB as being critical for ribosomal recruitment, with Arg235 being the most important (23, 24). The structures of RTA in complex with C-terminal peptides of the P2 protein ("P2C11" and "P2C10") were solved recently (25, 26). The structures revealed a mostly hydrophobic pocket on RTA formed by residues Tyr183, Arg235, Phe240, and Ile251 as the target of the P2 peptides. Short peptides corresponding to the P2 C terminus bind RTA with micromolar affinities (~200–450 μM) and prevent RTA depurination of intact ribosomes, without interfering with the active site (27). Thus, the large hydrophobic face of RTA normally occluded by RTB is apparently "repurposed" in the cytoplasm to assist in recruitment to the ribosome.

* For correspondence: Nicholas J. Mantis, nicholas.mantis@health.ny.gov; Michael J. Rudolph, mrudolph@nysbc.org.

Intracellular neutralization of ricin

In this study, we report the identification and characterization of 11 alpaca-derived single-domain antibodies (V_HHs) that recognize distinct epitopes on the hydrophobic surface of RTA normally occluded by RTB. We solved the cocrystal structures of four V_HHs (V9E1, V9F9, V9B2, and V9F6) bound to RTA, revealing that three of the four antibodies not only physically occlude the ribosomal P-stalk binding pocket on RTA but also mimic key P-stalk peptide interactions. The fourth V_HH, V9F6, recognizes an epitope adjacent to but not overlapping the ribosomal P-stalk binding pocket. Only the V_HHs that directly obstruct the ribosomal P-stalk binding pocket neutralized RTA in cell-free translation assays and blocked RTA–P2 peptide interactions. Finally, we show that transient expression of V9E1 and other V_HHs as intracellular antibodies ("intrabodies") renders Vero cells resistant to ricin toxin challenge to levels equivalent to that previously achieved with V_HHs targeting the active site of RTAs (28). Our findings support a model in which the interaction of RTA with ribosomal P-stalk proteins is a prerequisite to SRL depurination and raise the possibility of developing therapeutics that target two distinct sites on RTA.

Results

Identification of a collection of V_HHs that target the hydrophobic face of RTA normally occluded by RTB

As part of a V_HH phage-display screening strategy targeting diverse epitopes on ricin toxin's A and B subunits (28–31), we identified 11 V_HHs that recognized RTA but not ricin holotoxin (Table 1). The V_HHs grouped into five families based on complementarity-determining region 3 (CDR3) amino acid sequences (Table 1). The binding affinities of the 11 V_HHs for RTA ranged from potent to ultrapotent, as determined by surface plasmon resonance (SPR) (Table 1 and Fig. S1). V_HHs in families 1, 2, and 5 (n = 4 total) had equilibrium dissociation constants (K_D) of ~0.1 nM (0.073–0.22 nM; Table 1) with on (k_a) and off (k_d) rates ranging from 3.5×10^6 to 6.5×10^6 M^{-1} s^{-1} and 2.2×10^{-4} to 1.3×10^{-3} s^{-1}, respectively. Six of the seven V_HHs in families 3 and 4 had ultrahigh affinities for RTA with estimated K_Ds of <0.03 nM, with on rates (k_a) ranging from 3.2×10^6 to 6.1×10^8 M^{-1} s^{-1} and off rates (k_d) too slow to be accurately measured by SPR with no dissociation observed up to 10 min after V_HH–RTA complex formation. The seventh V_HH (V9D12) had a K_D of ~0.07 nM.

The reactivity of the V_HHs with RTA but not ricin holotoxin suggested that the V9 series of V_HHs might recognize the face of RTA that is normally occluded by RTB. In support of this notion, the V_HHs failed to recognize a derivative of RTA (RVEc) that lacks the folding domain (residues 200–267) that normally associates with RTB (Fig. S2). Moreover, we performed competition ELISAs with two monoclonal antibodies (mAbs) (SyH7 and JD4) that recognize epitopes on opposite sides of the RTA–RTB interface (Table 1 and Fig. S3) (32). V9E1, the sole V_HH in family 1, was not competed by either SyH7 or JD4, whereas V_HHs in families 2 (n = 1), 3 (n = 1), and 4 (n = 6) were competed by SyH7 but not JD4. The two V_HHs in family 5 were competed by JD4 but not SyH7. Thus, the five V_HH families fall within three distinct competition groups that likely represent spatially distinct epitopes on the "underside" of RTA that is exposed only when RTA is liberated from RTB and translocated, across the ER membrane into the cell cytoplasm.

We next evaluated the 11 V_HHs for toxin-neutralizing activity (TNA) in a cytotoxicity assay in which ricin was mixed with each V_HH across a range of antibody concentrations (0.01–1000 nM) and applied to Vero cells for 2 h. The cells were then washed to remove unbound antibody, and cell viability was measured 48 h later. As anticipated, none of the V9 V_HHs had any measurable TNA in this assay, even at >1000-fold molar excess over ricin. In contrast, V5E1, a previously described V_HH with potent TNA, neutralized ricin with an IC_{50} of ~5 nM (Fig. S2) (33). We conclude that the V9 V_HHs lack TNA in a conventional Vero cell cytotoxicity assay.

Structural analysis of V_HH–RTA complexes

We employed X-ray crystallography to identify the epitopes on RTA recognized by representative V_HH family members. Toward this end, the structures of four V_HHs (V9E1, V9B2, V9F9, and V9F6) complexed with RTA were solved at resolutions ranging from 1.3 to 2.3 Å (Table 2 and S1 and S2). Each V_HH assumed a typical immunoglobulin fold that consisted of nine β-strands arranged in two β-sheets comprised of five and four β-strands, with the exception of V9E1 as the first β-strand in V9E1's four β-strand sheet formed a loop instead of a β-strand. CDRs 1, 2, and 3 were located on one face of each V_HH molecule, and each V_HH antibody contained two, three,

Table 1
Summary of V9 V_HH families identified in this study

Family	V_HH	Competition		K_D (nM)	CDR3	GenBank
		SyH7	JD4			
1	V9E1	–	–	0.11	AADRDRLPSAITYEYNY	MW389192
2	V9E5	+	–	0.075	AGDRDTTAQAMGLFGARGDY	MW389193
3	V9B2	+	–	<0.03	ATEEVCTLGIFGHGPDDY	MW389188
4	V9B8	+	–	<0.03	AAADPLPLICTEADEYNY	MW389189
4	V9D12	+	–	0.070	AAADPLPLICTEPDEYTY	MW389191
4	V9E9	+	–	<0.03	AAADPLPLICTEADEYNY	MW389194
4	V9F9	+	–	<0.03	AAADPLPLVCTWGDEYDY	MW389196
4	V9G11	+	–	<0.03	AAADPLPLLCTEADEYDY	MW389198
4	V9H10	+	–	<0.03	AAADPLPLICTEADEYNY	MW389199
5	V9F6	–	+	0.22	AAGSYAAILYAPSY	MW389195
5	V9D5	–	+	0.073	AAGSYAAILYAPSY	MW389190

Underline indicates V_HHs whose structures were solved in complex with RTA in this study.

Table 2
V_HH–RTA binding data and interface information

V_HH	K_d[a]	EC_{50}[a]	H-bonds[b]		SB[c]	SC[d]	Total BSA[e]
			Total	CDR1/2/3			
V9B2	<0.03	43.0	2	1/0/1	5	0.72	1897
V9F9	<0.03	19.1	5	1/3/1	7	0.70 (0.73[f])	2028 (1994[f])
V9E1	0.11	4.0	9	0/1/5	6	0.61	1864
V9F6	0.22	1.9	11	5/2/4	0	0.73	1130

[a] Nanometer, determined in *in vitro* translation assay.
[b] Hydrogen bonds.
[c] Salt bridges.
[d] Shape complementarity.
[e] Buried surface area.
[f] Second V_HH–RTA complex in crystallographic asymmetric unit.

or four 3_{10} helices (Fig. 1). In all four V_HH–RTA complexes, CDR elements 1 to 3 made contact with RTA, although the interaction was invariably dominated by CDR3. V_HHs V9B2, V9F6, and V9F9 exhibited the canonical disulfide bond between Cys-22 and Cys-96 (Cys-22 and Cys-95 in V9F9) linking FR1 and FR3 (34). The analogous disulfide bond was absent in V9E1, despite the presence of the requisite cysteine residues. V9B2 and V9F9 each had a second less common disulfide bridge between CDR2 with CDR3: residues Cys-50 and Cys-102 in V9B2 and Cys-49 and Cys-105 in V9F9. The structure of RTA in each complex consisted of seven α-helices (A–G), up to three 3_{10} helices (3_{10a}–3_{10c}), and 10 β-strands (a–j). Specific RTA secondary structure annotations are shown in Fig. S4 for reference.

Among the four V_HH–RTA structures solved, V9B2–RTA and V9E1–RTA were most similar to each other, as evidenced by an RMSD of 1.8 Å over 352 Cα atoms. By comparison, V9B2–RTA had an RMSD of 2.0 Å over 347 Cα atoms with V9F9–RTA, whereas V9E1–RTA and V9F9–RTA had an RMSD of 2.0 Å over 305 Cα atoms (Fig. S5). The most dissimilar structure was V9F6–RTA as V9F6 principally interacted with a structurally distinct RTA epitope. No conformational changes were evident in RTA when bound by antibody, as RTA in all four V_HH–RTA complexes had RMSD values of 0.4 to 0.6 Å when all RTA Cα atoms were superimposed on RTA (Protein Data Bank [PDB] ID: 1RTC).

Occlusion of ribosomal P-stalk binding site of RTA

Three of the four V_HHs (V9E1, V9B2, and V9F9), representing families 1, 3, and 4, recognized epitopes that overlap with the ribosomal P-stalk binding pocket of RTA (Figs. 2 and S5, *A* and *B*). Specifically, V9B2, V9E1, and V9F9 engaged RTA α-helix F (residues 183–194), β-strand i and j, and loop i–j (residues 232–236 and residues 240, 242, and 244) as well as helix 3_{10}c (residues 246–249). V9E1 in addition contacts loop G–i on RTA (residue 223). The three V_HHs make slightly different contacts outside the P-stalk binding pocket, including with RTA α-helix A (residues 18, 19, 22–23, and 26), loop b–c (residue 41), loop E–F (residue 182), loop F–g (residue 196), α-helix G (residues 203 and 207), and several residues in helix 3_{10}c (residues 250–251), and immediately C-terminal to helix 3_{10}c (residue 253).

V9F6, in contrast, does not contact the P-stalk protein binding site (Figs. 2 and S5*C*). The epitope of V9F6 principally involves the C-terminal portion of α-helix A (residues 26, 29–30), loop–b (residues 34–37), β-strand b (residues 38–39), loop b–c (residues 40–41), β-strand c (residue 43), loop E–F (residue 182), and two residues in helix 3_{10}c (residues 249–250) as well as residues immediately proximal to helix 3_{10}c (residues 253, 261–262). That said, V9F6 does share a few contact points with the epitopes of V9B2, V9E1, and V9F9, including RTA α-helix A (residue 26), loop b–c (residue 41), loop E–F (residue 182), and residues 246, 249 to 250 within

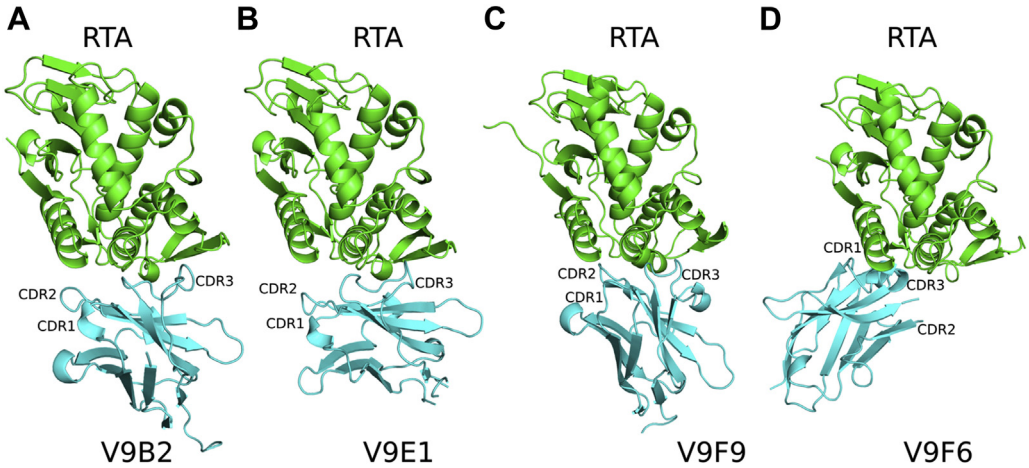

Figure 1. Structures of V_HH–RTA complexes. Structures of RTA (*green*) in complex with (*A*) V9B2, (*B*) V9E1, (*C*) V9F9, and (*D*) V9F6 depicted as *ribbon diagrams*. Each V_HH is colored *cyan*. RTA, ricin toxin subunit A.

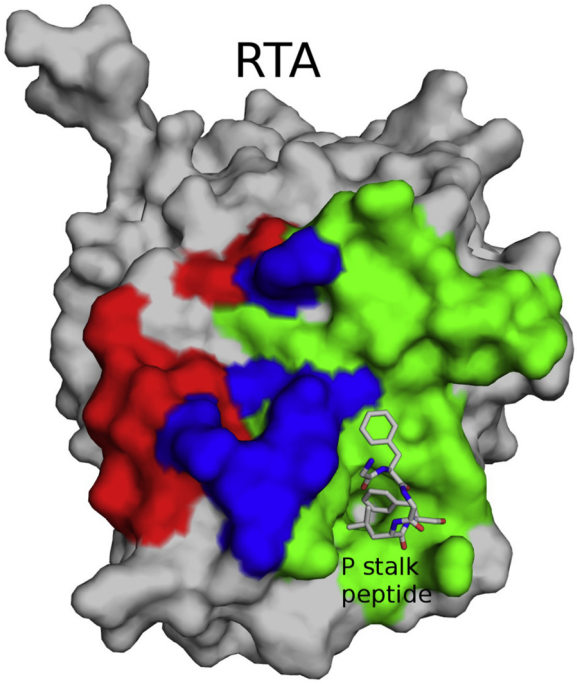

Figure 2. Relative localization of V9F6, V9B2, V9E1, and V9F9 epitopes on RTA. Molecular surface of RTA (*gray*) with the *red surface* highlighting the V9F6 epitope and the *green surface* depicting the combined epitopes of V9B2, V9E1, and V9F9. The *blue surface* depicts the overlapping epitopes of all four V_HHs. The P-stalk peptide highlighting the P-stalk binding site is drawn as *gray sticks* with carbon atoms *gray*, nitrogen atoms *blue*, and oxygen atoms *red*. RTA, ricin toxin subunit A.

helix 3_{10}c, along with residue 253 located immediately C-terminal to helix 3_{10}c (Fig. 2).

Detailed analysis of V_HH interactions with the ribosomal P-stalk binding pocket of RTAs

The interface between V9B2 and RTA buries 1897 Å^2 and consists of two hydrogen bonds and five salt bridges (Table 2). The two hydrogen bonds form between the carbonyl oxygen atoms of Asp-31 in CDR1 and Arg-193 in RTA, along with the carbonyl oxygen atom from Phe-107 in CDR3 and Arg-235 of RTA. The five salt bridges occur between CDR1 Asp-31 and RTA Arg-193, CDR2 Arg-57 with RTA Glu-41, CDR3 Asp-100 with RTA Arg-189, and Arg-193 along with CDR3 Asp-112 with RTA-Arg196 (Fig. 3*A*). V9B2s CDR3 residue Phe-107 also forms a key π-stacking interaction between RTA residues Tyr-183 and Phe-240. This interaction mimics the π-stacking interaction that occurs between RTA residues Tyr-183 and Phe-240 with Phe-10 in the ribosomal P-stalk peptide (sequence SDDDMGFGLFD), as revealed in the RTA–P-stalk peptide crystal structure (Figs. 4*A* and S6*B*) (35). Further similarities include V9B2 CDR3 residue Ile-106 that burrows into a hydrophobic patch on RTA lined by Val-242, Ile-247, and Leu-248, in a similar fashion to Leu-9 within the P-stalk peptide in complex with RTA (Figs. 4*A* and S6*A*). V9B2 has a shape complementary (Sc) score of 0.72 with RTA.

The interface between V9E1 and RTA buries 1864 Å^2 and involves nine hydrogen bonds and six salt bridges (Table 2). Two key hydrogen bonds are present between CDR3 residues Ile-106 and Tyr-108 with RTA residues Arg-234 and Arg-235, respectively. FR residue Glu-43 and CDR3 residue Glu-109 established two salt bridges with RTA residues Arg-234 and Arg-235, respectively (Fig. 3*B*). Arg-234 and Arg-235 are significant in that they form salt bridges with the C-terminal Asp residue in the P-stalk protein when bound to RTA (PDB ID: 5GU4) (Fig. S6*C*). V9E1 also inserts CDR3 residue Ile-106 between RTA residues Tyr-183 and Phe-240 similarly to P-stalk peptide residue Phe-10 (Fig. 4*B*). V9E1 has an Sc score of 0.62 with RTA.

The interface between V9F9 and RTA buries 2028 Å^2 (1994 Å^2 for the second V9F9–RTA complex within the crystallographic asymmetric unit) and consists of five hydrogen bonds and seven salt bridges, with contributions from each CDR. V9F9 CDR1 residue Asp-29 forms a salt bridge with RTA residue Arg-193, CDR2 residue Ser-53 H-bonded with RTA residue Glu-185, and CDR3 residue Asp-99 H-bonded with RTA residue Thr-190. Two salt bridges were also evident between V9F9 CDR3 residue Glu-110 and RTA residues Arg-234 and Arg-235 (Fig. 3*C*). As noted previously, Arg-234 and Arg-235 form key contacts with the P-stalk peptide residue Asp-11 (Fig. S6*C*). Finally, V9F9 CDR3 residue Leu-103 also mimics P-stalk peptide residue Phe-10 inserting between RTA residues Tyr-183 and Phe-240 (Fig. 4*C*). V9F9 has an Sc score of 0.70 with RTA (0.73 for the second V9F9–RTA complex within the crystallographic asymmetric unit).

V9F6 established a total of 11 hydrogen bonds between CDR1, CDR2, and CDR3 residues in V9F6 with RTA. Some of the key interactions included hydrogen bonding between the amide proton in CDR1 Arg-27 with the main-chain carbonyl oxygen of Ala-36 in RTA, the amide proton in CDR2 Leu-53 with Glu-41 in RTA, the amide proton in CDR3 Tyr-101 with the main-chain carbonyl oxygen of Glu-41 in RTA, and Tyr-110 with the main-chain carbonyl oxygen of Ala-36 in RTA (Fig. 3*D*). V9F6 does not contact the P-stalk protein binding site on RTA (Figs. 2 and S5*C*). In fact, the closest V9F6 residue Tyr-101 is 6.0 Å away from the N-terminal amine nitrogen atom of the superpositioned P-stalk peptide bound to RTA (Fig. 4*D*). Overall, the focal point of V9F6's interaction with RTA centers on β-strands b and c, loop b and c, and α-helix A with the rest of the antibody angling away from V9B2, V9E1, and V9F9 when bound to RTA (Fig. S5). V9F6 has an Sc score of 0.73.

Inhibition of RTA's RIP activity in vitro

The overlap between V9B2, V9F9, and V9E1's epitopes with the ribosomal P-stalk binding site on RTA prompted us to examine whether the V_HHs interfere with the RIP activity of RTA. We were particularly interested in the comparison between V9E1 and V9F6 because the two V_HHs have similar binding affinities for RTA, but V9E1 blocks the P-stalk binding site on RTA, whereas V9F6 does not.

To address this experimentally, the two V_HHs were assessed for their ability to neutralize RTA in an established *in vitro* translation (IVT) assay (28). Specifically, V9E1 and V9F6 were incubated with increasing amounts of RTA (0.02–13.6 nM)

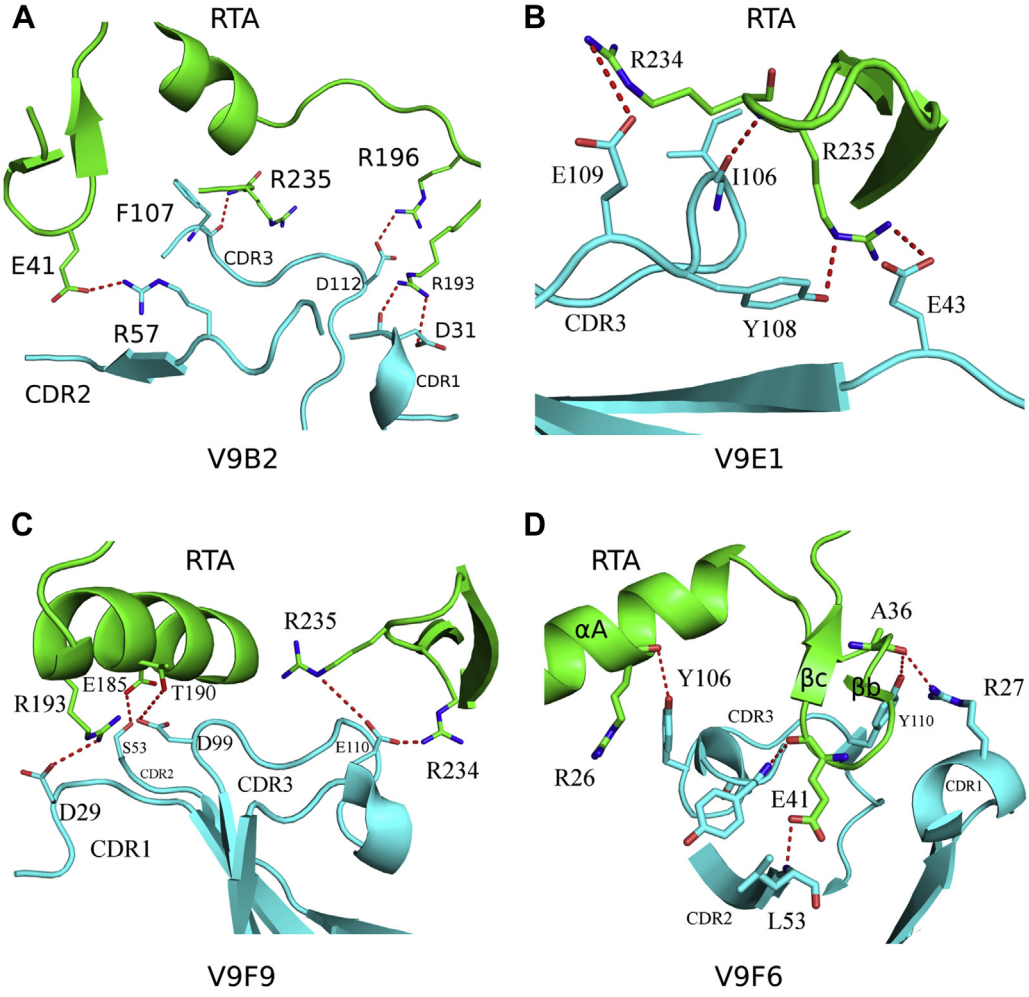

Figure 3. Close-up of the V_HH interactions with RTA. Zoom in of the interface between the ribbon diagrams of RTA (*green*) in complex with (*A*) V9B2, (*B*) V9E1, (*C*) V9F9, and (*D*) V9F6 depicting key V_HH contacts with RTA. Interacting V_HH and RTA residues are drawn as *sticks* and color coordinated to their respective main-chain color with nitrogen atoms *blue* and oxygen atoms *red*. Hydrogen bonds and salt bridges are represented as *red dashes*. RTA, ricin toxin subunit A.

and then added to a master mixture containing mRNA template encoding firefly luciferase (Fig. 5*A*). In the absence of RTA, the reaction yielded $>10^6$ relative light units, whereas the addition of RTA resulted in a dose-dependent reduction in translation, as evidenced by >1000-fold reduction in luciferase activity (Fig. S7). The addition V9F6 to the IVT assay had little to no effect on the RIP activity of RTA. In contrast, the addition of V9E1 (13.6 nM) resulted in a significant restoration of relative light unit, as compared with RTA treatment alone (Fig. 5*B*). In fact, V9E1's activity was similar to that of V2A11, a high-affinity V_HH (K_D = 0.31 nM) that occupies the active site of RTA (data not shown) (28). We conclude that V9E1 can indeed neutralize the RIP activity *in vitro* of RTA.

Inhibition of RTA–P2 stalk recognition in vitro

To test whether V9E1 interferes with the ability of RTA to associate with ribosome P-stalk proteins, we developed a solid phase binding assay in which microtiter plates were coated with a P2C11 peptide–bovine serum albumin BSA conjugate (BSA–P2C11) and then probed with RTA in the absence or the presence of antibody (Fig. 6). The addition of V9E1 resulted in a dose-dependent reduction of RTA attachment to BSA–P2C11 (Fig. 6). In fact, V9E1's EC_{50} corresponded to a 2:1 RTA:V_HH stoichiometry, whereas RTA binding to BSA–P2C11 was fully abolished at a 1:1 RTA:V_HH stoichiometry. In contrast, V9F6 had no effect on the ability of RTA to interact with BSA–P2C11, even when the antibody was in molar excess. These results are consistent with predictions from the crystal structures in that V9E1 blocks access of RTA to the ribosomal P-stalk proteins, whereas V9F6, whose epitope is slightly offset vis a vis the ribosomal P-stalk binding site on RTA, has no effect.

V9E1 intrabodies render Vero cells resistant to ricin intoxication

While V9E1 had no detectable ricin toxin neutralizing activity when applied to Vero cells extracellularly, we postulated that it might protect cells if expressed within the cell cytoplasm where it can encounter free RTA prior to engagement with the ribosome. In a recent study, we developed a protocol to successfully express RTA-specific V_HHs as intracellular antibodies or "intrabodies" in Vero cells (28, 36). Using that approach, the V9E1 and V9F6 coding sequences were cloned

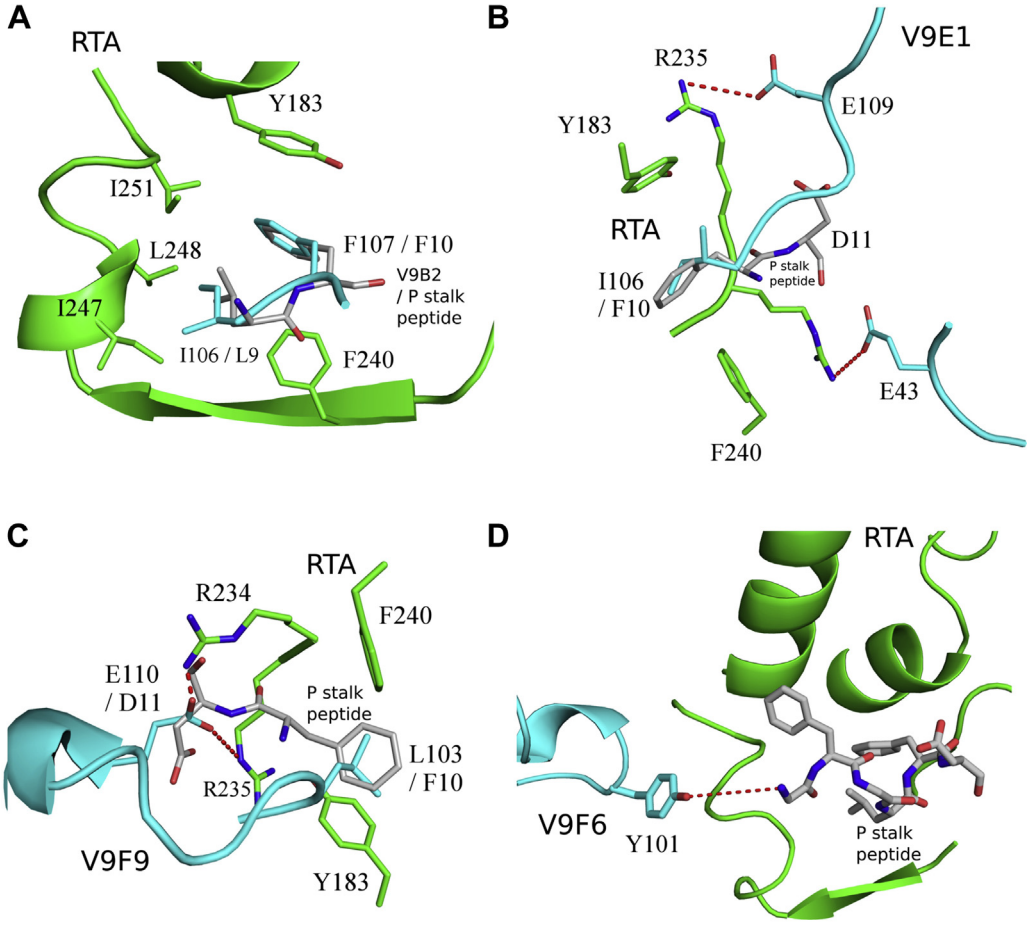

Figure 4. V_HH interactions with the P-stalk binding site. Close-up view of the *ribbon diagrams* of RTA (*green*) in complex with (*A*) V9B2, (*B*) V9E1, (*C*) V9F9 depicting key V_HH contacts with the P-stalk peptide, and (*D*) V9F6 highlighting the distant position of V9F6 relative to P-stalk binding site on RTA. Interacting V_HH and RTA residues are drawn as *sticks* and color coordinated to their respective main-chain color with nitrogen atoms *blue* and oxygen atoms *red*. The P-stalk peptide is drawn as *gray sticks* with carbon atoms *gray*, nitrogen atoms *blue*, and oxygen atoms *red*. Hydrogen bonds and salt bridges are represented as *red dashes*. RTA, ricin toxin subunit A.

into the mammalian expression vector pcDNA3 and delivered into Vero cells by lipid nanoparticle (LNP) transfection. Both V9E1 and V9F6 were detected in cell lysates at comparable levels, as determined using an RTA-capture ELISA (Fig. S8).

To assess the impact of the V9E1 and V9F6 intrabodies on the sensitivity of Vero cells to ricin intoxication, transiently transfected cells were treated with escalating amounts of ricin toxin for 2 h, washed, and then assessed for viability 48 h later (Fig. 7). A botulinum neurotoxin–specific V_HH, ciA-H7, was used as a control for these studies (37). Vero cells transfected with V9E1 were ~100-fold more resistant to ricin, as compared with cells transfected with LNP. In contrast, Vero cells transfected with V9F6 remained as sensitive to ricin as control cells (Fig. 7). This result demonstrates that targeting the ribosomal P-stalk binding site of RTA is sufficient to protect the ribosomes from ricin's RIP activity.

Inactivation of RTA by the remaining V9 families of V_HHs

We next turned our attention to the other V9 V_HH family members (Table 1). V9B2 and V9F9 (families 3 and 4) were of particular interest because they occlude the ribosome P-stalk binding site of RTA like V9E1 but bind RTA with significantly higher affinity (Table 1 and Fig. 4). As predicted, V9B2 and V9F9 inhibited RTA from binding to P2C11 in a dose-dependent manner (Fig. S9). Three other V_HHs from family 4 (V9B8/V9E9/V9G11) also prevented RTA–P2C11 interactions, whereas V9D5, a member of family 5, did not (Fig. S9). Similarly, in the IVT assay, there was a clear hierarchy of RTA neutralization, with V9B2 and V9F9 and other V_HHs in family 4 (V9B8/V9E9/V9G11) being the most potent inhibitors, followed by V9E1 and V9E5 (families 1 and 2) (Fig. 8). In contrast, V9D5 (family 5) was ineffective at neutralizing RTA in the IVT assay. These results further demonstrate that direct obstruction of, and not just proximity to, the ribosomal recruitment site of RTA is necessary to block P2 stalk binding and to neutralize RTA RIP activity.

From these experiments, we expected that, when expressed as intrabodies, V9B2 and V9F9 and three other V_HHs in family 4 would be more effective than V9E1 at protecting Vero cells from ricin intoxication. To test this hypothesis, Vero cells were transiently transfected with pcDNA3 expression vectors encoding families 3 and 4 V_HHs (V9B2, V9B8, V9E9, V9F9, and V9G11) and then challenged with ricin toxin 1 day later.

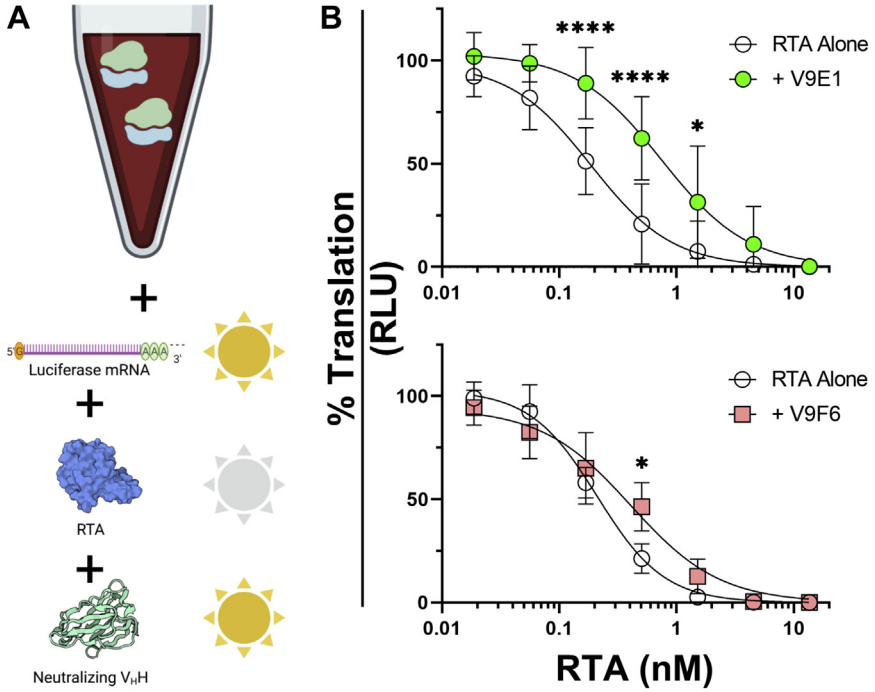

Figure 5. Inhibition of RIP activity by V_HHs targeting the ribosomal P-stalk binding pocket of RTA. *A, in vitro* translation assays were performed by mixing 13.6 nM V_HH with serial dilutions of RTA and then adding to a mixture containing rabbit reticulocyte lysate and luciferase mRNA. *B*, a standard curve (*open circles*) was established absent V_HH addition. Shown are the results and nonlinear regression analyses of each V_HH (*filled circles* or *squares*) normalized to positive controls without RTA added (100%). Data represent the mean ± SD of three (V9F6) or nine (V9E1) biological replicates. Significance was determined at each RTA concentration by two-way ANOVA. ****$p < 0.0001$, ***$p < 0.001$, **$p < 0.01$, *$p < 0.05$. RIP, ribosome-inactivating protein; RTA, ricin toxin subunit A.

While each of the V_HHs rendered Vero cells more resistant to ricin than the mock-transfected cells, their activities were lower than anticipated considering their ultra–high-binding affinities (Fig. 9). In fact, area under the curve (AUC) analysis indicated that V9E1 (family 1) was superior to V_HHs in families 3 and 4 (data not shown). V_HHs in families 3 and 4 differ from V9E1 (family 1) in that they have (or are suspected to have) a second disulfide bond that tethers CDR2 and CDR3, which could reduce protein expression (Fig. S10) (34).

To examine this experimentally, Vero cells were transfected as noted previously, and then cell lysates were subjected to RTA ELISA. As predicted, V9B2 was expressed at low levels, as compared with V_HHs in families 1, 2, and 5 (Fig. S8). Indeed, all five V_HHs with a predicted second disulfide bond were expressed at low levels (Fig. S8). Nonetheless, V9B2-transfected cells were significantly more resistant to ricin, as compared with control cells, revealing that even small amount of antibody has the capacity to neutralize ricin (Fig. 9).

Finally, we evaluated V9E5 (family 2) and V9D5 (family 5) as intrabodies. Neither V9E5 nor V9D5 contain a second disulfide bond, and, correspondingly, both expressed well in transfected cells (Fig. S8). V9E5-transfected cells were significantly resistant to ricin compared with LNP cells (>22-fold increase in EC_{50}), whereas V9D5 transfection conferred no protection from the toxin (Fig. 9).

Correlation between epitope specificity and binding affinity in RTA inhibition

With the recent discovery of the P-stalk binding site and demonstration that preventing P-stalk binding reduces the enzymatic activity of RTA, there is interest in developing small molecules against RTA that target P-stalk binding site (38). Those approaches have yielded compounds with high specificity that mimic interactions of Phe-10 within the P2C11 peptide and RTA as revealed by structural analysis, similar to the mimicry we observed for V9B2, V9E1, and V9F9. These molecules are also capable of inhibiting the depurination activity of RTA and can reduce ricin cytotoxicity in a Vero cell model, albeit at high concentrations because of their low affinities for RTA. From our structural and functional analyses, we reasoned that the primary drivers for recruitment site–targeted neutralization are binding strength, proximity to the P-stalk binding site, and the ability to express intracellularly. With this in mind, we reasoned that a competition assay with V9B2, an ultra–high-affinity RTA binder that overlaps P2C6 binding on RTA, would enable accurate prediction of the neutralization strength of inhibitors targeting the P-stalk binding site.

In this assay, V9B2 was coated on the ELISA plate, and each potential competitor V_HH was serially diluted and mixed with a fixed concentration of RTA (0.46 nM). There was a clear separation of V_HH competition profiles into three clusters with unique binding site and strength differences, as predicted (Fig. S11). Ultra–high-affinity V_HHs in families 3 and 4 (V9B2, V9B8, V9E9, V9F9, and V9G11) competed strongly with V9B2 as evidenced by 50% binding inhibition at 1:1 V_HH:RTA ratios. Next, V9E1 and V9E5, high-affinity V_HHs in families 1 and 2, competed more weakly with V9B2 for RTA with IC_{50} values at >25:1 V_HH:RTA ratios. Conversely, neither of the high-affinity

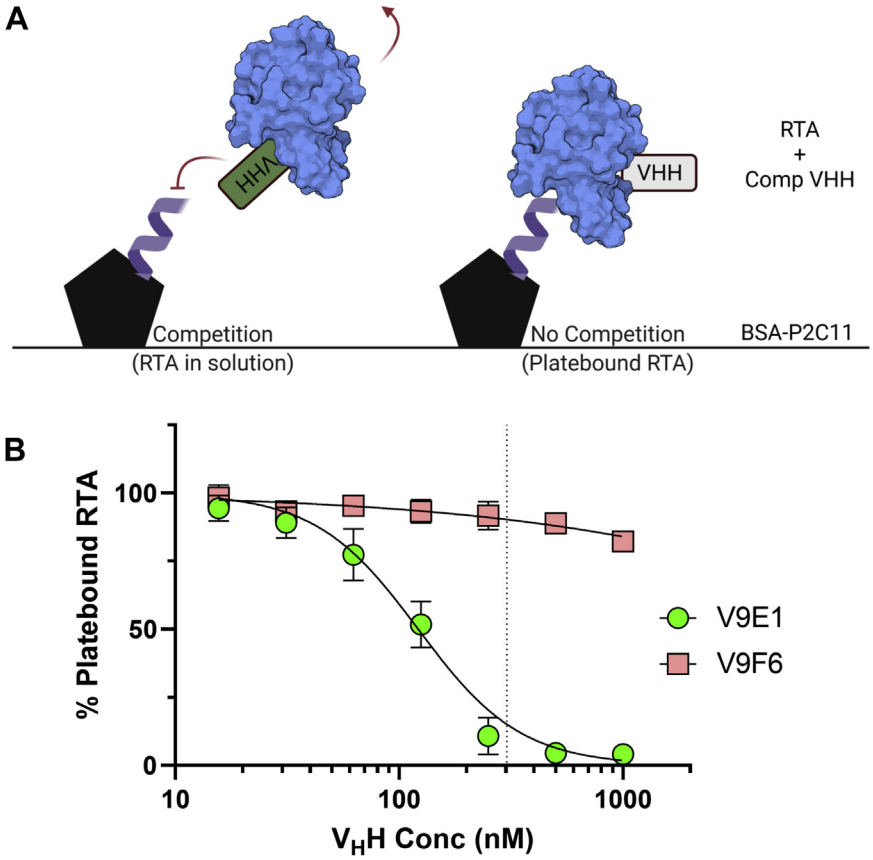

Figure 6. V9E1 but not V9F6 prevents RTA-stalk binding. *A*, schematic of the RTA-stalk competition ELISA. *B*, RTA (303 nM) was incubated with serial dilutions of either V9E1 or V9F6 and added to BSA–P2C11-coated ELISA plates. Platebound RTA was detected with a noncompeting monoclonal antibody and normalized to control wells without V_HH added (100%). *Vertical dotted line* indicates the 1:1 M ratio of RTA:V_HH added to the plate. Each point represents the mean ± SD of three (V9F6) or four (V9E1) biological replicates. BSA–P2C11, P2C11 peptide–bovine serum albumin BSA conjugate; RTA, ricin toxin subunit A.

V_HHs in family 5 (V9F6 and V9D5) demonstrated notable competition, likely because of the fact that their epitopes are offset relative to the P-stalk binding pocket. AUC analyses of these data correlate strongly with cell-free RTA neutralization results using a simple linear regression model, showing an apparent delineation of these three clusters by both V9B2 competition and IVT results (Fig. S11). Multiple linear regression analysis accurately predicted intrabody-based ricin resistance from each of the nine V9 V_HHs examined. To correct for expression level differences, we incorporated V9B2 competition data as well as intrabody expression data into this analysis. We observed a strong correlation (r^2 = 0.84) between both ELISAs and cytotoxicity results (Fig. S11). These results demonstrate that intracellular neutralization of the toxin by targeting the ribosomal recruitment event of RTA can be strongly predicted based on binding site specificity and affinity.

Discussion

The efficiency by which RTA inactivates mammalian ribosomes is remarkable. The underlying chemistry involves hydrolysis of a single N-glycosidic bond of a conserved adenosine residue situated in the SRL of 28S rRNA (9). The catalytic center of RTA constitutes a solvent-exposed cleft on one side of the molecule that accommodates a protruding adenine base. While the molecular basis of the depurination reaction has been recognized for decades, only recently have we gained insight into how RTA is recruited to the ribosome in the first place (19, 24, 25, 39–41). Indeed, there is now compelling evidence that the RIP activity of RTA is actually a two-step event, wherein step 1 involves interactions with ribosome by P-stalk proteins before the second engagement with the SRL. The X-ray crystal structures of RTA in a complex with peptides derived from human P2 stalk protein revealed a putative ribosomal P-stalk binding pocket located on the opposite side of the molecule relative to the active site (25, 26, 35). Genetic and biochemical studies had already implicated this exact region of RTA as being important in associating with purified ribosomes (21, 41, 42). However, the importance of the P-stalk binding event within the context of intoxicated mammalian cells has remained unclear.

The results of our current study reveal that ribosome P-stalk binding is an essential step in the RIP activity of RTA. This conclusion is based on the demonstration that surgically targeting the ribosomal P-stalk binding pocket on RTA with high-affinity single-domain antibodies was sufficient to knock out the RIP activity of RTA in cell-free assays, as well as within the context of intoxicated cells. The comparison between two V_HHs, V9E1 and V9F6, proved especially informative. V9E1 and V9F6 have comparable binding affinities for RTA (0.11 and 0.22 nM, respectively) but slightly different epitopes

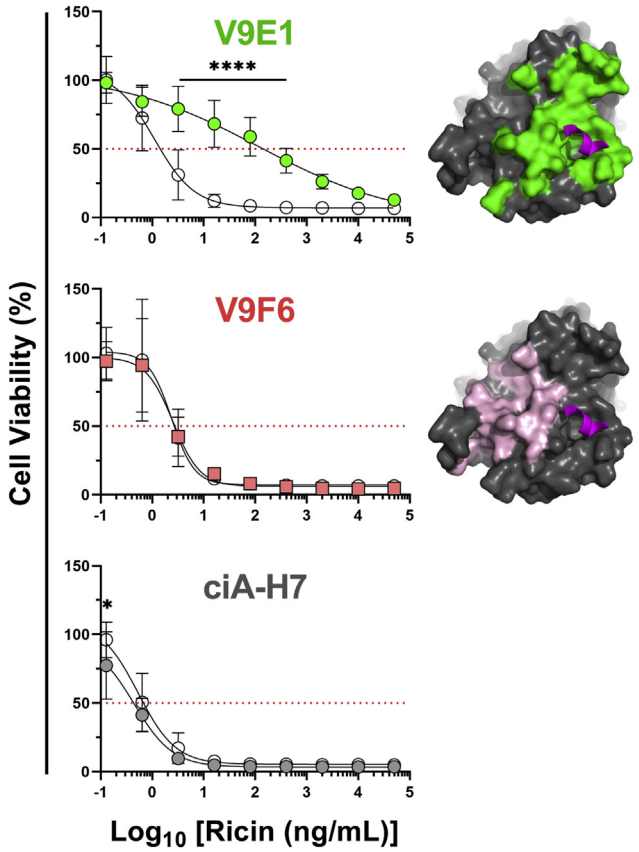

Figure 7. Protection of Vero cells from ricin by intracellular V9E1. Vero cells were seeded in 96-well plates for 1 day and then transiently transfected with V_HH intrabodies. Cells were treated with dilutions of ricin 1 day after transfection, and viability was assessed 2 days post-treatment. *Left*, viabilities of cells transfected with vehicle control (LNP; *open circles*) or intrabodies (*filled circles* or *squares*) were measured as a percentage of "live" control cells not treated with ricin. Shown are the mean ± SD of at least three biological replicates representing three technical replicates each. In the absence of a BoNT-specific ELISA, expression of ciA-H7 intrabody was confirmed by Western blot (data not shown). Significance was determined at each ricin concentration by two-way ANOVA. ****$p < 0.0001$, ***$p < 0.001$, **$p < 0.01$, *$p < 0.05$. *Right*, epitopes on RTA highlighted for V9E1 (*green*) and V9F6 (*pink*) with the stalk peptide shown in *magenta*. BoNT, botulinum neurotoxin; LNP, lipid nanoparticle; RTA, ricin toxin subunit A.

relative to the P-stalk binding site. V9E1 occludes the P-stalk binding pocket and forms hydrogen bonds and π-stacking interactions with residues (*e.g.*, Arg234, Arg235, Tyr183, and Phe240) involved in P-stalk peptide recognition (25, 35). V9F6, by comparison, recognizes an epitope immediately adjacent to but not obstructing the P-stalk binding pocket. The relatively small difference in epitope location had significant consequences in terms of interfering with RTA activity: V9E1 inhibited RTA–P2C11 interactions, whereas V9F6 did not. V9E1 protected ribosomes from RTA in cell-free translation assays, whereas V9F6 did not. Finally, V9E1 conferred resistance to ricin toxin when expressed as an intrabody in Vero cells, whereas V9F6 did not. These results demonstrate that direct occlusion of the ribosomal P-stalk peptide binding site is sufficient to neutralize the RIP activity of RTA within the cell cytoplasm. Moreover, they suggest that ribosomal P-stalk protein interactions are likely confined to a relatively small surface area on RTA (*i.e.*, essentially outlined by the footprint of V9E1).

Moreover, blocking access to the P-stalk binding pocket of RTA attenuates the RIP activity of RTA to a degree equivalent to that achieved by interfering with the active site of RTA. This conclusion is based on the comparison of V9E1 with V2A11. V2A11 is one of seven V_HHs identified that target the active site pocket of RTA (28). The binding affinity of V2A11 for RTA is similar to V9E1 (0.11 nM *versus* 0.31 nM). The two antibodies have identical Sc scores (Sc = 0.61) and similar buried surface areas (1953 *versus* 1864 $Å^2$). In the cell-free translation assays, V2A11 and V9E1 had identical RTA inhibition values, and, when comparing across studies of RTA, similar profiles in terms of conferring resistance to ricin toxin when expressed as intrabodies in Vero cells. In essence, docking with the ribosomal P-stalk proteins is a requisite step in the RIP activity, and as others have proposed, as important as the actual depurination event itself (21, 22, 42, 43).

In many ways, the two-step model, as put forth by Tumer *et al.* (21), explains the efficiency of RTA as a RIP. A long-standing question in the field is how RTA, following unfolding and translocation across the ER membrane, finds its substrate within the densely packed environment of the cell cytoplasm. Molecular chaperones like Hsc70 have been proposed to engage RTA following ER dislocation, whereas others have suggested that refolding may be facilitated by ribosomes themselves (44, 45). Irrespective of the how and where the folding event occurs, the sheer efficiency of RTA as a ribotoxin indicates that it wastes no time in accessing its substrate. Imai *et al.* (46) recently provided evidence that P-stalk proteins function as "factor-pooling platforms" that increase the local concentration of translational GTPases ("EFs") near the ribosome surface to ensure optimal translation efficiency. Seemingly, RTA exploits (and competes for) the pathways used by EFs to engage with the GTPase-associated center and increase likelihood of encountering the SRL. This strategy may be conserved considering that other RIPs, such as Shiga toxin 2, have also been shown to bind to the C-terminal domain of ribosome P-stalk proteins (47).

While our focus up to this point has been on V9E1, it is just one of the nine V_HHs identified in this study capable of neutralization of RTA in the IVT assay and interfering with RTA–P2C11 association. Structural analysis of two of those additional V_HHs, namely V9B2 and V9F9, revealed occupancy of ribosome P-stalk binding pocket of RTA in a manner similar to V9E1. Six of the nine V_HHs (including V9B2 and V9F9) are remarkable in that their binding affinities for RTA were estimated to be in the low picomolar range (<0.03 nM). With extremely slow off-rates, V9B2 and V9F9 (and the other V_HHs) were expected to be exceptionally potent inhibitors of ricin toxin when expressed as intrabodies. While they did render Vero cells more resistant to ricin than controls, the levels were not commensurate with binding affinities. As it turns out, V9B2 and V9F9 (as well as others) expressed poorly as intrabodies, most likely because of the fact that they carry a second noncanonical disulfide bond between CDR2 and CDR3. Indeed, it is generally recognized that V_HHs and single-chain variable

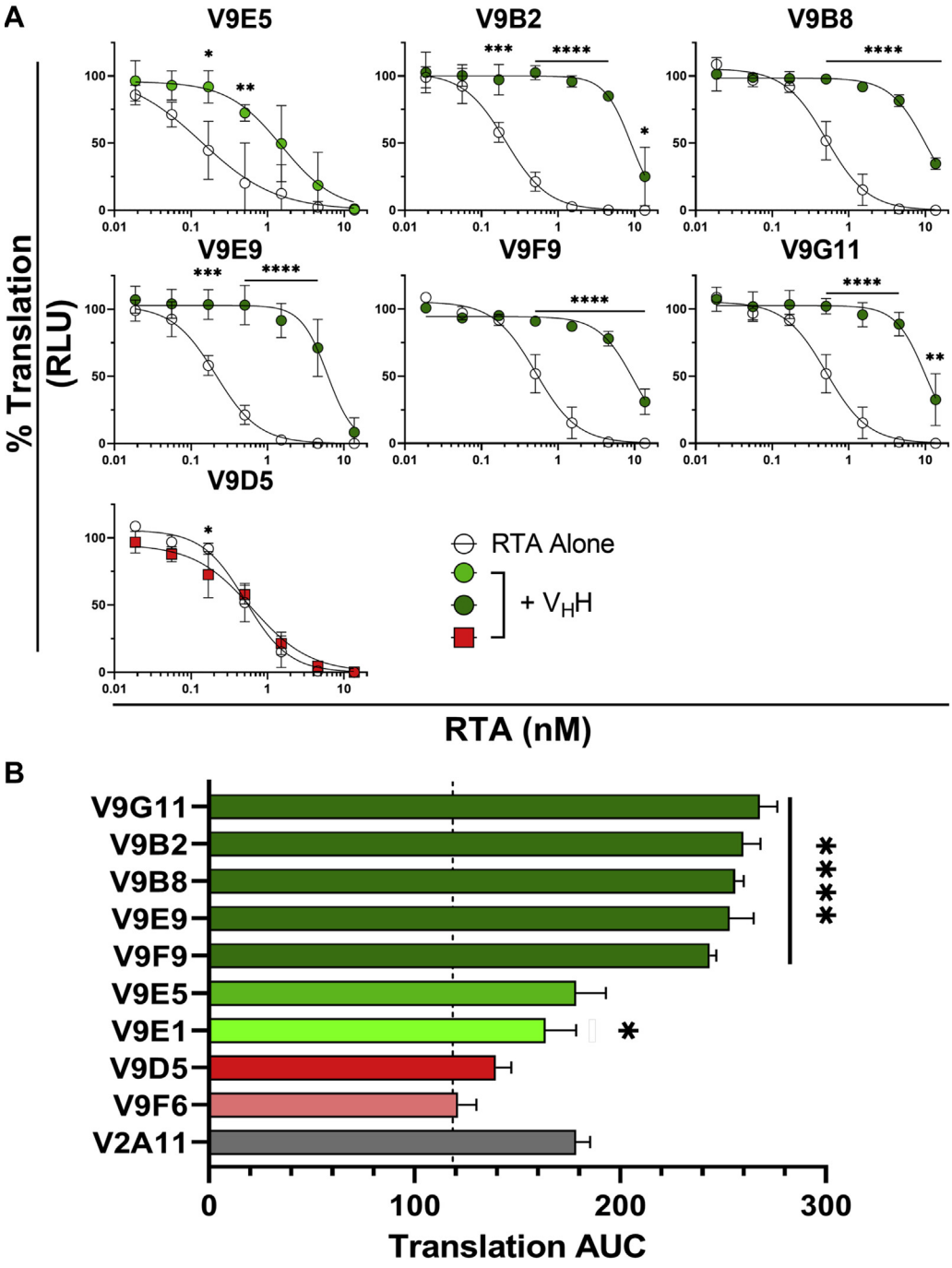

Figure 8. Inhibition of the activity of RTA by V_HH families 2, 3, and 4. *A, in vitro* translation assays were performed with V_HHs from families 2, 3, 4, and the remaining family 5 V_HH (V9D5). Shown are mean ± SD of three replicate experiments. Significance at each RTA concentration was determined by two-way ANOVA. *B*, dose–response curves for each V_HH–RTA combination were transformed, and area under the curve (AUC) analysis was performed. The *dashed line* represents the standard curve AUC (x = 118). The high-affinity active site V_HH, V2A11, is also shown (*gray*). Significance was calculated using a one-way ANOVA with comparisons to the standard curve AUC shown. ****$p < 0.0001$, ***$p < 0.001$, **$p < 0.01$, *$p < 0.05$. RTA, ricin toxin subunit A.

fragments carrying a second disulfide bond are poorly expressed because of the reducing environment of the cytoplasm (48, 49). Our preliminary efforts to engineer out the pertinent cysteine residues in V9B2 and V9F9 using methodologies described by others have proven unsuccessful to date (T. Czajka, unpublished results) (49, 50).

The remarkably high-binding affinities reported here for six of the V9 V_HHs are certainly unusual but not unprecedented in the case of ricin toxin or other agents (33). For example, several V_HHs with picomolar affinities for the spike protein of severe acute respiratory syndrome coronavirus 2 were isolated from immune camelid libraries (51, 52). There are likely multiple factors that give rise of such tight binders, including a hydrophobic target interface and the addition of noncanonical disulfide bonds within CDR elements that minimize the entropic cost of antigen

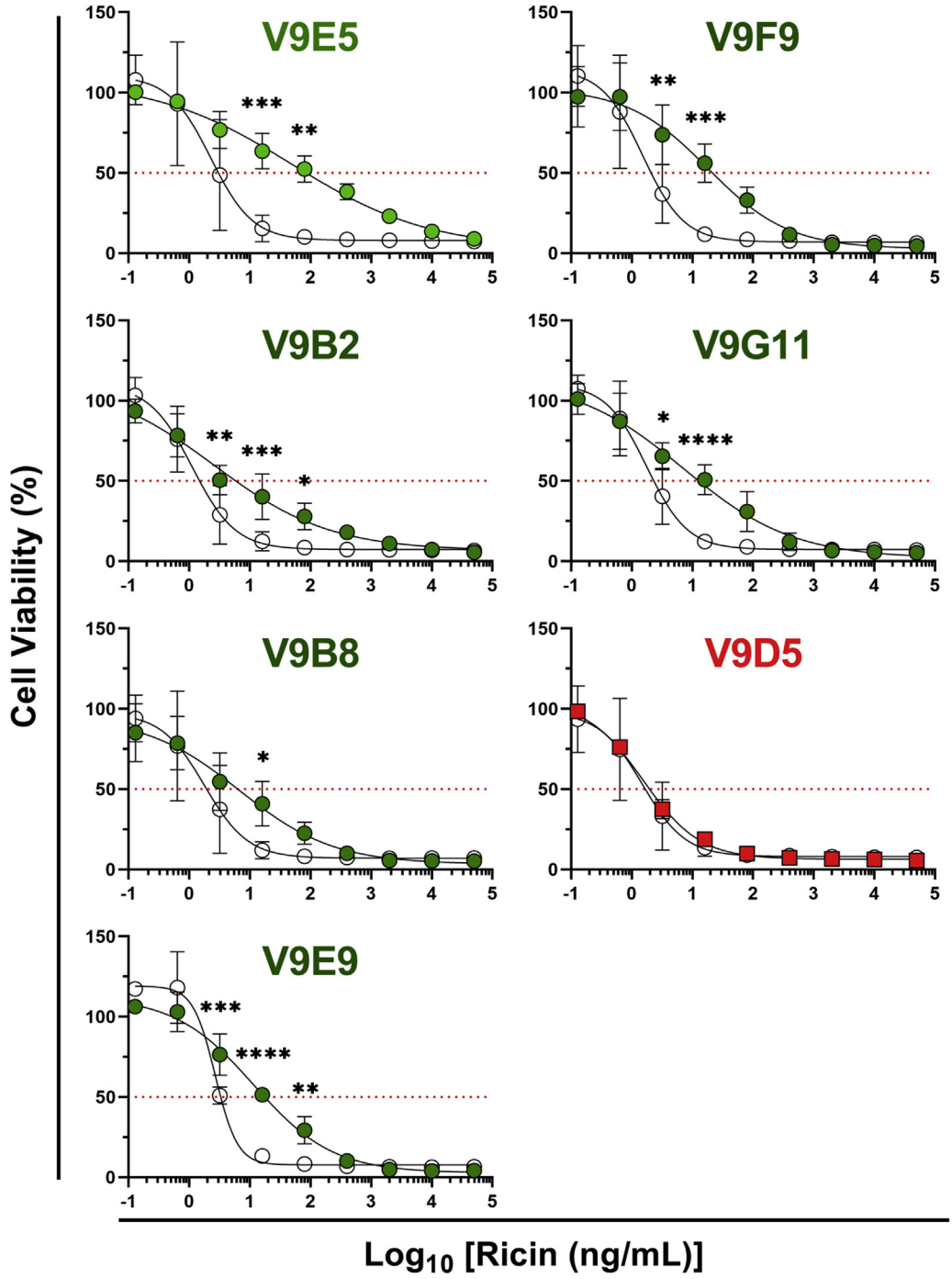

Figure 9. Protection of Vero cells from ricin by family 2, 3, and 4 intrabodies. Cytotoxicity assays were performed with intrabodies from families 2, 3, 4, and the remaining family 5 intrabody (V9D5). Viabilities of cells transfected with vehicle control (LNP; *open circles*) or intrabodies (*filled circles* or *squares*) were measured as a percentage of "live" control cells not treated with ricin. Shown are the mean ± SD of at least three biological replicates representing three technical replicates each. Significance was determined at each ricin concentration by two-way ANOVA. ****$p < 0.0001$, ***$p < 0.001$, **$p < 0.01$, *$p < 0.05$. LNP, lipid nanoparticle.

engagement (53, 54). The relative binding affinities of V_HHs can be further enhanced through oligomerization as dimers, trimers, or even higher order oligomers (55–57). Toward this end, we have found that the potency of V9E1–V2A11 heterodimers greatly exceeds that of any single V_HH monomer tested to date (T. Czajka and N. Mantis, manuscript in preparation). Such constructs if delivered by mRNA technologies may offer an entirely new strategy for ricin toxin postexposure therapeutics (58).

Experimental procedures

Chemicals and biological reagents

Ricin toxin (*R. communis* agglutinin II; RCA_{60}) and RTA were purchased from Vector Laboratories and dialyzed against

PBS to remove residual sodium azide prior to use in cytotoxicity assays. Unless noted otherwise, all reagents were purchased from Sigma–Aldrich.

V_HH ELISAs

Anti-RTA mAbs were coated in 96-well plates at a concentration of 1 μg/ml in PBS overnight at 4 °C. Plates were then blocked with 2% goat serum in PBS containing 0.1% Tween-20 (PBST) for 2 h at room temperature. Ricin, RTA, or RVEc was then applied to the plates at 1 μg/ml to be captured by the anti-RTA antibodies for 1 h, and unbound protein was washed away with PBST. V_HHs were then applied at a concentration of 330 nM in PBS for 1 h. Unbound V_HH was washed away with PBST, and bound V_HH was detected for 1 h with an anti-E-horseradish peroxidase (HRP) secondary antibody (Bethyl Labs). 3,3′,5,5′-Tetramethylbenzidine (TMB; SureBlue; SeraCare) was used to develop the plates and was then quenched with 1 M phosphoric acid. Absorbance at 450 nm was read on a VersaMax microplate reader (Molecular Devices).

Cloning, expression, and protein purification for structural analysis

The PCR amplicons for the four V_HHs were subcloned into the pSUMO expression vector encoding an N-terminal decahistidine and SUMO tag. RTA (residues 1–268) was subcloned into the N-terminally decahistidine-tagged MCSG7 expression vector. All cloning were performed using a standard ligase-independent cloning protocol. All V_HHs and RTA were expressed in *Escherichia coli* strain BL21(DE3)-pRARE. The transformed bacteria were grown at 37 °C in terrific broth medium and induced at 20 °C with 0.1 mM (IPTG) at an absorbance at 600 nm of 0.6 for ∼16 h at 20 °C. After induction, cells were harvested and resuspended in 20 mM Hepes (pH 7.5) and 150 mM NaCl. The cell suspension was sonicated and centrifuged at 30,000*g* for 30 min. After centrifugation, the protein-containing supernatant was purified by nickel-affinity and size-exclusion chromatography on an AKTAxpress System (GE Healthcare), which consisted of a 1 ml nickel affinity column followed by a Superdex 200 16/60 gel filtration column. The elution buffer consisted of 0.5 M imidazole in binding buffer, and the gel filtration buffer consisted of 20 mM Hepes (pH 7.5), 150 mM NaCl, and 20 mM imidazole. Fractions containing each V_HH and RTA were pooled and subject to tobacco etch virus protease cleavage (1:10 weight ratio) for 3 h at room temperature in order to remove their respective fusion tags. The cleaved proteins were passed over a 1 ml Ni–NTA agarose (Qiagen) gravity column to remove tobacco etch virus protease, cleaved residues, and uncleaved fusion protein. To generate each V_HH–RTA protein complex, RTA was mixed with each V_HH in a 1:1 stoichiometry then concentrated to 10 mg/ml.

Crystallization and data collection

V_HH–RTA crystals were grown by sitting drop vapor diffusion at 20 °C using a protein to reservoir volume ratio of 1:1 with total drop volume of 0.2 μl. Crystallization solutions are shown in Table S1. Crystals were flash frozen in liquid nitrogen after a short soak in the respective crystallization buffers supplemented with 25% ethylene glycol. Data were collected at the 24-ID-C and 24-ID-E beamlines at the Advanced Photon Source, Argonne National Labs. All data were indexed, merged, and scaled using HKL2000 (59) and then converted to structure factors using CCP4 (60).

Structure determination and refinement

The V_HH–RTA complex structures were solved by molecular replacement using the program Phaser (61). Molecular replacement calculations were performed using the coordinates of the ricin A chain as a search model for RTA (PDB ID: 1RTC) in all four V_HH–RTA complexes. The V_HH coordinates used as a search model for all four V_HH–RTA complexes were D10 (PDB ID: 4LGR) or A9 (PDB ID: 6CWG) with all three of the CDRs removed from the search model. The resulting phase information from molecular replacement was used to autobuild the polypeptide chain of the V_HH within each complex using automated refinement procedure (62). Further manual model building was performed with the open source software, Coot (63), combined with structural refinement employing the PHENIX package (64). Data collection and refinement statistics are listed in Table S2. Molecular graphics were prepared using PyMOL (Schrodinger, DeLano Scientific LLC).

P2C11 peptide competition

To evaluate V_HH/ribosomal stalk competition for RTA binding, 96-well ELISA plates (Immulon 4HBX) were coated overnight at 4 °C with 10 μg/ml of BSA–P2C11 (Genemed Synthesis, Inc) in PBS. Plates were blocked with PBS containing goat serum (2% v/v) and Tween-20 (0.1% v/v) for 2 h at room temperature. During block, RTA (303 nM) was incubated with twofold serial dilutions of V_HH in 96-well dilution plates for 30 to 60 min with 12 wells per plate receiving only RTA and block buffer to serve as 100% binding controls. Following block, V_HH–RTA samples were transferred to the ELISA plates for 1 h. 1 μg/ml PB10 (anti-RTA mAb) (reference) was added for 1 h followed by HRP-conjugated goat antimouse immunoglobulin G secondary antibody (1:2000 dilution; SouthernBiotech) for 30 min. TMB (SureBlue; Kirkegaard & Perry Labs) was added for 6 to 10 min followed by stop solution (1 M phosphoric acid). ELISA plates were analyzed using a SpectraMax iD3 spectrophotometer equipped with Softmax Pro 7 software (Molecular Devices) at an absorbance at 450 nm. Unbound RTA, PH12, and 2° antibody were removed after each incubation period by washing plates with PBS-Tween (0.1%). RTA, V_HHs, and antibodies were diluted in block buffer.

V9E1 and V9B2 competition assays

96-Well ELISA plates were coated overnight at 4 °C with 1 μg/ml of V9E1 or V9B2 in PBS. Competition ELISAs were performed as described for the stalk competition, with the exception of the RTA and V_HH concentrations. During block, RTA (4.6 nM for V9E1 competition or 0.46 nM for V9B2 competition) was incubated with threefold serial dilutions of

V_HH in 6-well dilution plates for 30 to 60 min with 12 wells per plate receiving only RTA and block buffer to serve as 100% binding controls.

Intrabody detection

Intrabody detection ELISAs were performed as described previously with minor alterations (28). 96-Well ELISA plates were coated overnight at 4 °C with the mAb PH12 (1 μg/ml in PBS) (65). Plates were washed and blocked for 2 h at room temperature. Following block, RTA (1 μg/ml in PBS) was applied to ELISA plates for 1 h. Transfected cell lysate was serially diluted in duplicate and added to plates for 1 h. Plates were washed and HRP-conjugated anti-E-tag antibody (1:10,000 dilution; Bethyl Laboratories; catalog no.; A190-132P) was applied for 1 h. Plates were washed, and 100 μl TMB was added for 5 to 10 min followed by stop solution. ELISA plates were analyzed using a SpectraMax iD3 spectrophotometer equipped with Softmax Pro 7 software at an absorbance at 450 nm. Purified V_HH protein with a C-terminal E-tag was used as a positive binding control for each transfection. Plates were washed following each step in PBS-Tween (0.1%). Cell lysates and secondary antibody were diluted in block buffer.

In vitro *RTA inhibition*

V_HHs at a stock concentration of 218.2 nM in dimethyl sulfoxide were diluted in 1% BSA in PBS (w/v) and mixed with threefold serial dilutions of RTA in PBS from 54.5 to 0.07 nM, to a final concentration of 13.6 nM V_HH and 13.6 to 0.019 nM RTA. This was added to an ice-cold mixture containing luciferase mRNA (3.7 μg/ml; Ambion, Inc) and Retic Lysate IVT Kit (Thermo Fisher Scientific). The cocktail was incubated for 90 min at 30 °C and then chilled on ice for 5 min before being transferred to wells of an opaque 96-well microtiter plate with an equal volume (20 μl) of Bright-Glo luciferase substrate (Promega) at room temperature. Luminescence was detected immediately using a SpectraMax iD3. Luciferase translation was determined as a percentage of positive control reactions without RTA added. Standard curves were generated for RTA dilutions with dimethyl sulfoxide, and no V_HH was added.

Vero cell culture, transfection, and lysis

Vero cells (American Type Culture Collection) were cultured in Dulbecco's minimal essential medium with fetal bovine serum (10% v/v) and penicillin/streptomycin at 37 °C (5% CO_2). For ELISAs and Western blotting, cells were transfected in 6-well plates and lysed 48 h after transfection, as described previously (28). For cytotoxicity assays, cells were transfected in 96-well plates and treated with ricin 24 h after transfection, as described (28). Viability was determined using Cell Titer-Glo (Promega) and a SpectraMax iD3 for luminescence detection. Viability was measured as a percentage of live control cells (transfected but not treated with ricin).

Statistical analysis

Statistical analyses were performed using GraphPad Prism 9.1 software (GraphPad Software, Inc) for Windows. For IVT assays, a one-way ANOVA was with the Tukey's post hoc test to compare areas under the curve for each condition, and a two-way ANOVA was used with the Sidak post hoc test to compare the percent translation between V_HH and the RTA standard curves at each RTA concentration. For intrabody ELISA expression analysis, a one-way ANOVA with the Tukey's post hoc test was used to compare each transfection condition. For intrabody cytotoxicity results, a two-way ANOVA was used with the Sidak post hoc test to compare transfected and LNP-vehicle control cell viabilities at each ricin concentration. A simple linear regression and Pearson correlation analysis were performed between the AUC data for competition ELISAs and IVT dose–response curves. To predict intrabody-based Vero cell protection, a multiple linear regression least-squares analysis was performed with cytotoxicity AUC as the dependent outcome and intrabody ELISA and V9B2 competition areas under the curve as independent variables.

PDB accession numbers

The structures generated in this study were deposited in the PDB (http://www.rcsb.org/pdb/) under accession numbers 7TGF for V9B2–RTA, 7TGI for V9E1–RTA, 7TH3 for V9F6–RTA, and 7TH2 for V9F9–RTA as described in Table S1.

Data availability

All data associated with the results presented in this article are included herein or within the supporting information.

Supporting information—This article contains supporting information.

Acknowledgments—We are grateful to Leslie Eisele and Renjie Song of the Wadsworth Center's Biochemistry and Immunology Core facility for assistance with SPR. We thank the staff in the Wadsworth Center's Media and Tissue Culture core for providing reagents, the Applied Genomics Technologies core for DNA sequencing. We thank members of the Mantis laboratory for technical assistance and Beth Cavosie for administrative support. Finally, we gratefully acknowledge the 24-ID-C and 24-ID-E beamline staff at the Advanced Photon Source for their assistance in data collection.

Author contributions—T. F. C., D. J. V., S. D., M. J. R., and N. J. M. conceptualization; T. F. C., D. J. V., M. J. R., and N. J. M. methodology; T. F. C., D. J. V., M. J. R., and N. J. M. software; T. F. C., D. J. V., and M. J. R. validation; T. F. C., D. J. V., M. J. R., and N. J. M. formal analysis; T. F. C., D. J. V., S. D., M. J. R., and N. J. M. investigation; T. F. C., D. J. V., and M. J. R. resources; M. J. R. data curation; T. F. C., D. J. V., M. J. R., and N. J. M. writing–original draft; T. F. C., D. J. V., M. J. R., and N. J. M. writing–review & editing; T. F. C., D. J. V., and M. J. R. visualization; M. J. R. and N. J. M. supervision; N. J. M. project administration; N. J. M. funding acquisition.

Funding and additional information—This work was supported by contract no. HHSN272201400021C and grant R01 AI125190 from the National Institute of Allergy and Infectious Diseases (National Institutes of Health). The content is solely the responsibility of the

authors and does not necessarily represent the official views of the National Institutes of Health. The funders had no role in study design, data collection and analysis, decision to publish, or preparation of the article.

Conflict of interest—The authors declare that they have no conflicts of interest with the contents of this article.

Abbreviations—The abbreviations used are: AUC, area under the curve; BSA–P2C11, P2C11 peptide–bovine serum albumin BSA conjugate; CDR, complementarity-determining region; EF, elongation factor; ER, endoplasmic reticulum; HRP, horseradish peroxidase; IVT, *in vitro* translation; LNP, lipid nanoparticle; mAb, monoclonal antibody; PBST, PBS containing 0.1% Tween-20; PDB, Protein Data Bank; RIP, ribosome-inactivating protein; RTA, ricin toxin A subunit; RTB, ricin toxin B subunit; Sc, shape complementary; SPR, surface plasmon resonance; SRL, sarcin–ricin loop; TMB, 3,3′,5,5′-tetramethylbenzidine; TNA, toxin-neutralizing activity.

References

1. Montfort, W., Villafranca, J. E., Monzingo, A. F., Ernst, S. R., Katzin, B., Rutenber, E., Xuong, N. H., Hamlin, R., and Robertus, J. D. (1987) The three-dimensional structure of ricin at 2.8 A. *J. Biol. Chem.* **262**, 5398–5403
2. Olsnes, S., Refsnes, K., and Pihl, A. (1974) Mechanism of action of the toxic lectins abrin and ricin. *Nature* **249**, 627–631
3. Sowa-Rogozinska, N., Sominka, H., Nowakowska-Golacka, J., Sandvig, K., and Slominska-Wojewodzka, M. (2019) Intracellular transport and cytotoxicity of the protein toxin ricin. *Toxins (Basel)* **11**, 350
4. Bellisola, G., Fracasso, G., Ippoliti, R., Menestrina, G., Rosen, A., Solda, S., Udali, S., Tomazzolli, R., Tridente, G., and Colombatti, M. (2004) Reductive activation of ricin and ricin A-chain immunotoxins by protein disulfide isomerase and thioredoxin reductase. *Biochem. Pharmacol.* **67**, 1721–1731
5. Nowakowska-Gołacka, J., Sominka, H., Sowa-Rogozińska, N., and Słomińska-Wojewódzka, M. (2019) Toxins utilize the endoplasmic reticulum-associated protein degradation pathway in their intoxication process. *Int. J. Mol. Sci.* **20**, 1307
6. Spooner, R. A., Watson, P. D., Marsden, C. J., Smith, D. C., Moore, K. A., Cook, J. P., Lord, J. M., and Roberts, L. M. (2004) Protein disulphide-isomerase reduces ricin to its A and B chains in the endoplasmic reticulum. *Biochem. J.* **383**, 285–293
7. Wesche, J., Rapak, A., and Olsnes, S. (1999) Dependence of ricin toxicity on translocation of the toxin A-chain from the endoplasmic reticulum to the cytosol. *J. Biol. Chem.* **274**, 34443–34449
8. Endo, Y., Mitsui, K., Motizuki, M., and Tsurugi, K. (1987) The mechanism of action of ricin and related toxic lectins on eukaryotic ribosomes. The site and the characteristics of the modification in 28 S ribosomal RNA caused by the toxins. *J. Biol. Chem.* **262**, 5908–5912
9. Endo, Y., and Tsurugi, K. (1987) RNA N-glycosidase activity of ricin A-chain. Mechanism of action of the toxic lectin ricin on eukaryotic ribosomes. *J. Biol. Chem.* **262**, 8128–8130
10. Iordanov, M. S., Pribnow, D., Magun, J. L., Dinh, T. H., Pearson, J. A., Chen, S. L., and Magun, B. E. (1997) Ribotoxic stress response: Activation of the stress-activated protein kinase JNK1 by inhibitors of the peptidyl transferase reaction and by sequence-specific RNA damage to the alpha-sarcin/ricin loop in the 28S rRNA. *Mol. Cell. Biol.* **17**, 3373–3381
11. Vind, A. C., Genzor, A. V., and Bekker-Jensen, S. (2020) Ribosomal stress-surveillance: Three pathways is a magic number. *Nucleic Acids Res.* **48**, 10648–10661
12. Carbone, C. E., Loveland, A. B., Gamper, H. B., Jr., Hou, Y. M., Demo, G., and Korostelev, A. A. (2021) Time-resolved cryo-EM visualizes ribosomal translocation with EF-G and GTP. *Nat. Commun.* **12**, 7236
13. Endo, Y., and Tsurugi, K. (1988) The RNA N-glycosidase activity of ricin A-chain. The characteristics of the enzymatic activity of ricin A-chain with ribosomes and with rRNA. *J. Biol. Chem.* **263**, 8735–8739
14. Ready, M. P., Kim, Y., and Robertus, J. D. (1991) Site-directed mutagenesis of ricin A-chain and implications for the mechanism of action. *Proteins* **10**, 270–278
15. Moazed, D., Robertson, J. M., and Noller, H. F. (1988) Interaction of elongation factors EF-G and EF-Tu with a conserved loop in 23S RNA. *Nature* **334**, 362–364
16. Monzingo, A. F., and Robertus, J. D. (1992) X-ray analysis of substrate analogs in the ricin A-chain active site. *J. Mol. Biol.* **227**, 1136–1145
17. Mlsna, D., Monzingo, A. F., Katzin, B. J., Ernst, S., and Robertus, J. D. (1993) Structure of recombinant ricin A chain at 2.3 A. *Protein Sci.* **2**, 429–435
18. Robertus, J. D., Yan, X., Ernst, S., Monzingo, A., Worley, S., Day, P., Hollis, T., and Svinth, M. (1996) Structural analysis of ricin and implications for inhibitor design. *Toxicon* **34**, 1325–1334
19. Grela, P., Szajwaj, M., Horbowicz-Drozdzal, P., and Tchorzewski, M. (2019) How ricin damages the ribosome. *Toxins (Basel)* **11**, 241
20. May, K. L., Yan, Q., and Tumer, N. E. (2013) Targeting ricin to the ribosome. *Toxicon* **69**, 143–151
21. Li, X. P., Chiou, J. C., Remacha, M., Ballesta, J. P., and Tumer, N. E. (2009) A two-step binding model proposed for the electrostatic interactions of ricin a chain with ribosomes. *Biochemistry* **48**, 3853–3863
22. May, K. L., Li, X. P., Martinez-Azorin, F., Ballesta, J. P., Grela, P., Tchorzewski, M., and Tumer, N. E. (2012) The P1/P2 proteins of the human ribosomal stalk are required for ribosome binding and depurination by ricin in human cells. *FEBS J.* **279**, 3925–3936
23. Jetzt, A. E., Cheng, J. S., Li, X. P., Tumer, N. E., and Cohick, W. S. (2012) A relatively low level of ribosome depurination by mutant forms of ricin toxin A chain can trigger protein synthesis inhibition, cell signaling and apoptosis in mammalian cells. *Int. J. Biochem. Cell Biol.* **44**, 2204–2211
24. Zhou, Y., Li, X. P., Chen, B. Y., and Tumer, N. E. (2017) Ricin uses arginine 235 as an anchor residue to bind to P-proteins of the ribosomal stalk. *Sci. Rep.* **7**, 42912
25. Fan, X., Zhu, Y., Wang, C., Niu, L., Teng, M., and Li, X. (2016) Structural insights into the interaction of the ribosomal P stalk protein P2 with a type II ribosome-inactivating protein ricin. *Sci. Rep.* **6**, 37803
26. Shi, W. W., Mak, A. N., Wong, K. B., and Shaw, P. C. (2016) Structures and ribosomal interaction of ribosome-inactivating proteins. *Molecules* **21**, 1588
27. Li, X. P., Kahn, J. N., and Tumer, N. E. (2018) Peptide mimics of the ribosomal P stalk inhibit the activity of ricin A chain by preventing ribosome binding. *Toxins (Basel)* **10**, 371
28. Rudolph, M. J., Czajka, T. F., Davis, S. A., Thi Nguyen, C. M., Li, X. P., Tumer, N. E., Vance, D. J., and Mantis, N. J. (2020) Intracellular neutralization of ricin toxin by single-domain antibodies targeting the active site. *J. Mol. Biol.* **432**, 1109–1125
29. Poon, A. Y., Vance, D. J., Rong, Y., Ehrbar, D., and Mantis, N. J. (2017) A supercluster of neutralizing epitopes at the interface of ricin's enzymatic (RTA) and binding (RTB) subunits. *Toxins (Basel)* **9**, 378
30. Rudolph, M. J., Poon, A. Y., Kavaliauskiene, S., Myrann, A. G., Reynolds-Peterson, C., Davis, S. A., Sandvig, K., Vance, D. J., and Mantis, N. J. (2021) Structural analysis of toxin-neutralizing, single-domain antibodies that bridge ricin's A-B subunit interface. *J. Mol. Biol.* **433**, 167086
31. Vance, D. J., Tremblay, J. M., Rong, Y., Angalakurthi, S. K., Volkin, D. B., Middaugh, C. R., Weis, D. D., Shoemaker, C. B., and Mantis, N. J. (2017) High-resolution epitope positioning of a large collection of neutralizing and nonneutralizing single-domain antibodies on the enzymatic and binding subunits of ricin toxin. *Clin. Vaccine Immunol.* **24**, e00236-17
32. Toth, R. T. I., Angalakurthi, S. K., Van Slyke, G., Vance, D. J., Hickey, J. M., Joshi, S. B., Middaugh, C. R., Volkin, D. B., Weis, D. D., and Mantis, N. J. (2017) High-definition mapping of four spatially distinct neutralizing epitope clusters on RiVax, a candidate ricin toxin subunit vaccine. *Clin. Vaccine Immunol.* **24**, e00237-17
33. Rudolph, M. J., Vance, D. J., Cassidy, M. S., Rong, Y., and Mantis, N. J. (2017) Structural analysis of single domain antibodies bound to a second

neutralizing hot spot on ricin toxin's enzymatic subunit. *J. Biol. Chem.* **292**, 872–883
34. Muyldermans, S. (2021) Applications of nanobodies. *Annu. Rev. Anim. Biosci.* **9**, 401–421
35. Shi, W. W., Tang, Y. S., Sze, S. Y., Zhu, Z. N., Wong, K. B., and Shaw, P. C. (2016) Crystal structure of ribosome-inactivating protein ricin A chain in complex with the C-terminal peptide of the ribosomal stalk protein P2. *Toxins (Basel)* **8**, 296
36. Czajka, T. F., and Mantis, N. J. (2022) Single-domain antibodies for intracellular toxin neutralization. *Methods Mol. Biol.* **2446**, 469–487
37. Tremblay, J. M., Kuo, C. L., Abeijon, C., Sepulveda, J., Oyler, G., Hu, X., Jin, M. M., and Shoemaker, C. B. (2010) Camelid single domain antibodies (VHHs) as neuronal cell intrabody binding agents and inhibitors of Clostridium botulinum neurotoxin (BoNT) proteases. *Toxicon* **56**, 990–998
38. Li, X. P., Harijan, R. K., Cao, B., Kahn, J. N., Pierce, M., Tsymbal, A. M., Roberge, J. Y., Augeri, D., and Tumer, N. E. (2021) Synthesis and structural characterization of ricin inhibitors targeting ribosome binding using fragment-based methods and structure-based design. *J. Med. Chem.* **64**, 15334–15348
39. Grela, P., Li, X. P., Horbowicz, P., Dźwierzyńska, M., Tchórzewski, M., and Tumer, N. E. (2017) Human ribosomal P1-P2 heterodimer represents an optimal docking site for ricin A chain with a prominent role for P1 C-terminus. *Sci. Rep.* **7**, 5608
40. Horbowicz-Drożdżal, P., Kamel, K., Kmiecik, S., Borkiewicz, L., Tumer, N. E., Shaw, P. C., Tchórzewski, M., and Grela, P. (2021) Phosphorylation of the conserved C-terminal domain of ribosomal P-proteins impairs the mode of interaction with plant toxins. *FEBS Lett.* **595**, 2221–2236
41. Zhou, Y., Li, X. P., Kahn, J. N., McLaughlin, J. E., and Tumer, N. E. (2019) Leucine 232 and hydrophobic residues at the ribosomal P stalk binding site are critical for biological activity of ricin. *Biosci. Rep.* **39**, BSR20192022
42. Li, X. P., Kahn, P. C., Kahn, J. N., Grela, P., and Tumer, N. E. (2013) Arginine residues on the opposite side of the active site stimulate the catalysis of ribosome depurination by ricin A chain by interacting with the P-protein stalk. *J. Biol. Chem.* **288**, 30270–30284
43. Chiou, J. C., Li, X. P., Remacha, M., Ballesta, J. P., and Tumer, N. E. (2008) The ribosomal stalk is required for ribosome binding, depurination of the rRNA and cytotoxicity of ricin A chain in Saccharomyces cerevisiae. *Mol. Microbiol.* **70**, 1441–1452
44. Argent, R. H., Parrott, A. M., Day, P. J., Roberts, L. M., Stockley, P. G., Lord, J. M., and Radford, S. E. (2000) Ribosome-mediated folding of partially unfolded ricin A-chain. *J. Biol. Chem.* **275**, 9263–9269
45. Spooner, R. A., Hart, P. J., Cook, J. P., Pietroni, P., Rogon, C., Hohfeld, J., Roberts, L. M., and Lord, J. M. (2008) Cytosolic chaperones influence the fate of a toxin dislocated from the endoplasmic reticulum. *Proc. Natl. Acad. Sci. U. S. A.* **105**, 17408–17413
46. Imai, H., Uchiumi, T., and Kodera, N. (2020) Direct visualization of translational GTPase factor pool formed around the archaeal ribosomal P-stalk by high-speed AFM. *Proc. Natl. Acad. Sci. U. S. A.* **117**, 32386–32394
47. Rudolph, M. J., Davis, S. A., Tumer, N. E., and Li, X. P. (2020) Structural basis for the interaction of Shiga toxin 2a with a C-terminal peptide of ribosomal P stalk proteins. *J. Biol. Chem.* **295**, 15588–15596
48. Seo, M. J., Jeong, K. J., Leysath, C. E., Ellington, A. D., Iverson, B. L., and Georgiou, G. (2009) Engineering antibody fragments to fold in the absence of disulfide bonds. *Protein Sci.* **18**, 259–267
49. Worn, A., and Pluckthun, A. (1998) An intrinsically stable antibody scFv fragment can tolerate the loss of both disulfide bonds and fold correctly. *FEBS Lett.* **427**, 357–361
50. Proba, K., Worn, A., Honegger, A., and Pluckthun, A. (1998) Antibody scFv fragments without disulfide bonds made by molecular evolution. *J. Mol. Biol.* **275**, 245–253
51. Guttler, T., Aksu, M., Dickmanns, A., Stegmann, K. M., Gregor, K., Rees, R., Taxer, W., Rymarenko, O., Schunemann, J., Dienemann, C., Gunkel, P., Mussil, B., Krull, J., Teichmann, U., Gross, U., *et al.* (2021) Neutralization of SARS-CoV-2 by highly potent, hyperthermostable, and mutation-tolerant nanobodies. *EMBO J.* **40**, e107985
52. Xiang, Y., Nambulli, S., Xiao, Z., Liu, H., Sang, Z., Duprex, W. P., Schneidman-Duhovny, D., Zhang, C., and Shi, Y. (2020) Versatile and multivalent nanobodies efficiently neutralize SARS-CoV-2. *Science* **370**, 1479–1484
53. Govaert, J., Pellis, M., Deschacht, N., Vincke, C., Conrath, K., Muyldermans, S., and Saerens, D. (2012) Dual beneficial effect of interloop disulfide bond for single domain antibody fragments. *J. Biol. Chem.* **287**, 1970–1979
54. Kunz, P., Zinner, K., Mucke, N., Bartoschik, T., Muyldermans, S., and Hoheisel, J. D. (2018) The structural basis of nanobody unfolding reversibility and thermoresistance. *Sci. Rep.* **8**, 7934
55. Czajka, T. F., Vance, D. J., and Mantis, N. J. (2020) Slaying SARS-CoV-2 one (single-domain) antibody at a time. *Trends Microbiol.* **29**, 195–203
56. Laursen, N. S., Friesen, R. H. E., Zhu, X., Jongeneelen, M., Blokland, S., Vermond, J., van Eijgen, A., Tang, C., van Diepen, H., Obmolova, G., van der Neut Kolfschoten, M., Zuijdgeest, D., Straetemans, R., Hoffman, R. M. B., Nieusma, T., *et al.* (2018) Universal protection against influenza infection by a multidomain antibody to influenza hemagglutinin. *Science* **362**, 598–602
57. Muyldermans, S. (2021) A guide to: Generation and design of nanobodies. *FEBS J.* **288**, 2084–2102
58. Thran, M., Mukherjee, J., Ponisch, M., Fiedler, K., Thess, A., Mui, B. L., Hope, M. J., Tam, Y. K., Horscroft, N., Heidenreich, R., Fotin-Mleczek, M., Shoemaker, C. B., and Schlake, T. (2017) mRNA mediates passive vaccination against infectious agents, toxins, and tumors. *EMBO Mol. Med.* **9**, 1434–1447
59. Otwinowski, Z., and Minor, W. (1997) Processing of X-ray diffraction data collected in oscillation mode. *Methods Enzymol.* **276**, 307–326
60. Winn, M. D., Ballard, C. C., Cowtan, K. D., Dodson, E. J., Emsley, P., Evans, P. R., Keegan, R. M., Krissinel, E. B., Leslie, A. G., McCoy, A., McNicholas, S. J., Murshudov, G. N., Pannu, N. S., Potterton, E. A., Powell, H. R., *et al.* (2011) Overview of the CCP4 suite and current developments. *Acta Crystallogr. D Biol. Crystallogr.* **67**, 235–242
61. McCoy, A. J., Grosse-Kunstleve, R. W., Adams, P. D., Winn, M. D., Storoni, L. C., and Read, R. J. (2007) Phaser crystallographic software. *J. Appl. Crystallogr.* **40**, 658–674
62. Morris, R. J., Perrakis, A., and Lamzin, V. S. (2003) ARP/wARP and automatic interpretation of protein electron density maps. *Methods Enzymol.* **374**, 229–244
63. Emsley, P., Lohkamp, B., Scott, W. G., and Cowtan, K. (2010) Features and development of Coot. *Acta Crystallogr. D Biol. Crystallogr.* **66**, 486–501
64. Adams, P. D., Afonine, P. V., Bunkoczi, G., Chen, V. B., Davis, I. W., Echols, N., Headd, J. J., Hung, L. W., Kapral, G. J., Grosse-Kunstleve, R. W., McCoy, A. J., Moriarty, N. W., Oeffner, R., Read, R. J., Richardson, D. C., *et al.* (2010) PHENIX: A comprehensive Python-based system for macromolecular structure solution. *Acta Crystallogr. D Biol. Crystallogr.* **66**, 213–221
65. Van Slyke, G., Angalakurthi, S. K., Toth, R. T. T., Vance, D. J., Rong, Y., Ehrbar, D., Shi, Y., Middaugh, C. R., Volkin, D. B., Weis, D. D., and Mantis, N. J. (2018) Fine-specificity epitope analysis identifies contact points on ricin toxin recognized by protective monoclonal antibodies. *Immunohorizons* **2**, 262–273